Expanded area metrology for tip-based wafer inspection in the nanomanufacturing of electronic devices

Tsung-Fu Yao
Liam G. Connolly
Michael Cullinan

Expanded area metrology for tip-based wafer inspection in the nanomanufacturing of electronic devices

Tsung-Fu Yao,[†] Liam G. Connolly,[†] and Michael Cullinan*
The University of Texas at Austin, Nanoscale Design and Manufacturing Laboratory, Walker Department of Mechanical Engineering, Austin, Texas, United States

Abstract. Effective measurement of fabricated structures is critical to the cost-effective production of modern electronics. However, traditional tip-based approaches are poorly suited to in-line inspection at current manufacturing speeds. We present the development of a large area inspection method to address throughput constraints due to the narrow field-of-view (FOV) inherent in conventional tip-based measurement. The proposed proof-of-concept system can perform simultaneous, noncontact inspection at multiple hotspots using single-chip atomic force microscopes (sc-AFMs) with nanometer-scale resolution. The tool has a throughput of ~60 wafers/h for five-site measurement on a 4-in. wafer, corresponding to a nanometrology throughput of ~66,000 μm^2/h. This methodology can be used to not only locate subwavelength "killer" defects but also to measure topography for in-line process control. Further, a postprocessing workflow is developed to stitch together adjacent scans measured in a serial fashion and expand the FOV of each individual sc-AFM such that total inspection area per cycle can be balanced with throughput to perform larger area inspection for uses such as defect root-cause analysis. © 2019 Society of Photo-Optical Instrumentation Engineers (SPIE) [DOI: 10.1117/1.JMM.18.3.034003]

1 Introduction

Nanoscale manufacturing methods have grown immeasurably in importance over the last two decades due to their significant role in the rapid scaling of semiconductor device transistor density and, thus, their ever-decreasing critical feature size, as first hypothesized by Moore.[1] However, methods to quickly inspect the fabricated structures, as is commonly done in micro- and macroscale manufacturing, have not kept pace.[2] Ideally, in-line inspection methods for nanoscale manufacturing processes such as photolithography and chemical–mechanical–polishing would be able to both rapidly detect defects and measure critical dimensions (CDs) over a full silicon wafer in a nondestructive fashion to build a defect map for process control and more thorough postproduction off-line review.[3,4] Off-line review can then resample a portion of the wafer according this defect map and provide higher resolution images to show more detailed information. Currently, optical, electron beam inspection (EBI), and atomic force microscopy (AFM) techniques are used to find "killer defects" in patterned wafers. But, as patterns shrink, inherent physical barriers such as the diffraction limits of visible light make optical methods ill-suited for this purpose.[2,4–7] CD-EBI and CD-AFM are alternative methods to image these devices beyond the diffraction limit. These methods provide superior resolution, down to sub-nm levels in some cases,[8] fulfilling the most challenging customer needs. Although these methods have already proven their capability at finding defects invisible to traditional optical inspection, and at measuring even the most exacting CDs at the current 7-nm node resolutions, the throughput in these systems is orders of magnitude less than that of traditional optical inspection—requiring hours for off-line review. Further, the small field-of-view (FOV) of these methods can limit their usefulness in inspection processes. Although expanded-area AFM tools have been developed, these large and costly tools still require huge amounts of time to scan the areas desired.[9] Therefore, it is typical in industry that the entirety of the wafer is never measured with EBI or AFM, as it would be a hugely time-consuming task, and only certain regions of interest where critical defects are most likely to exist or where CDs are most important, known as "hotspots," are evaluated. This type of hotspot inspection relies on a premade map, which is generally derived using a pattern simulation tool. By inspecting only small regions, it is possible to determine, with various statistical methods, if there are critical variations occurring in the manufacturing process that might affect the final performance of a fabricated device.[3,10] Unfortunately, due to the low throughput of EBI and classical AFM tools, it is difficult to inspect more than one small hotspot in-line without delaying the entire production line. Therefore, new techniques are needed that can measure several points across a wafer with nanoscale accuracy and a high enough throughput to avoid decreasing manufacturing productivity. In most cases, this necessitates a speed of at least 60 wafers per hour (WPH).

This study presents a prototype of a new tip-based system capable of measuring multiple hotspots across a wafer simultaneously and with nanometer-scale precision. This in-line inspection system uses AFMs with all the necessary actuators and sensors built into a single-microelectromechanical system (MEMS) chip to drastically reduce probe footprint and allow multiple AFMs to be arrayed together at a high density for concurrent multipoint measurement.[11–13] The in-line hotspot inspection strategy using these single chip

---

*Address all correspondence to Michael Cullinan, E-mail: Michael.Cullinan@austin.utexas.edu

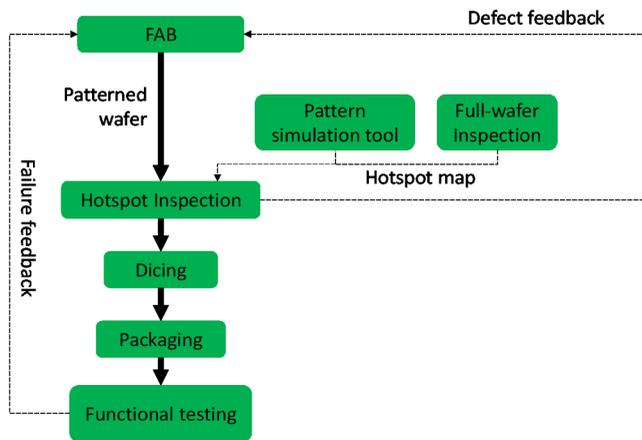†These authors share first authorship.

Fig. 1 Workflow for in-line hotspot inspection strategy and schematic layout of multisite "hotspot" metrology over a 4-in. wafer area.
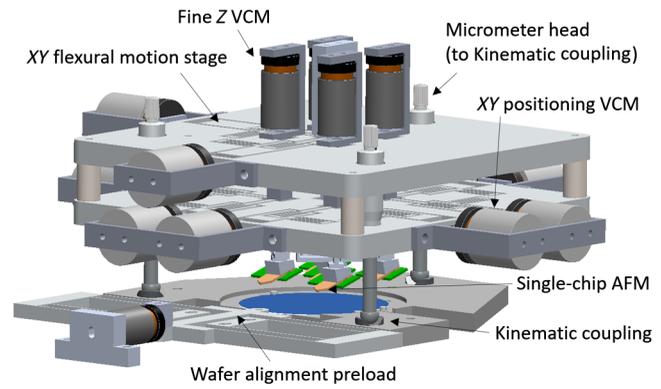

Fig. 2 CAD rendering of the proposed in-line wafer metrology tool consisting of multiple sc-AFMs attached to individual approach mechanism and actuators all positioned in the $X-Y$ plane by VCMs. The entire motion-inspection stage can be lifted from the wafer alignment and capture stage for fast wafer loading and unloading.

AFMs (sc-AFMs) is outlined in Fig. 1. In this workflow, a premade hotspot map is first generated either through full-wafer inspection of an out-of-line sample wafer or by using a pattern simulation tool. This hotspot map is then used to determine where to position the sc-AFMs over the wafer before measurements are taken. Once the inspection locations are set, each wafer exiting a given manufacturing step can be run through the hotspot inspection tool to rapidly determine if the process is changing or drifting out-of-control over time. The inspection data from every wafer can then be fed back to a centralized controller for the patterning or fabrication operations enabling it to modify process parameters and maximize process yield—all in real time. A tool following this new sc-AFM-based, parallel measurement methodology would be ideal to improve the existing hybrid metrology structure commonly utilized in semiconductor manufacturing where optical methods are used to rapidly locate large defects or indirectly measure collections of features such as in scatterometry, and CD-EBI and AFM are reserved for longer, off-line single- and sub-nm precision measurement of CDs. The proposed system fills the gap left between in-line optical inspection and out-of-line CD inspection, providing direct, high-throughput measurements of subwavelength defects and sample topography.

2 System Architecture

2.1 Overview of Proposed System

The proposed in-line wafer inspection system consists of five sc-AFMs (ICSPI Corp.) attached to individual approach mechanisms paired to voice coil motor (VCM) magnetic force actuators. Each approach mechanism sits on its own independent XY positioning stage as shown in Fig. 2. This allows each sc-AFM to be individually positioned and approached to take measurements no matter the topography of the sample being measured. This system architecture also enables expansion of each sc-AFM's FOV through coordinated use of the individual XY positioning stages for each chip, allowing for successive scans to be stitched together in postprocessing to create large-area measurements. The system also includes a wafer repositioning subsystem, which aligns sc-AFM tips to the wafer to achieve submicron repeatability and thus guarantees minimal offset (compared with 20-μm^2 FOV of the sc-AFM) for each wafer loaded during

inspection.[12] This passive alignment system uses kinematic couplings to align the AFM stage to the wafer stage and a three-pin alignment system to passively align the wafer to the wafer stage. These passive alignment elements help to ensure that features of interest are directly positioned under the AFM tips every time a new wafer is loaded into the system so that measurements can be made rapidly and efficiently.[14]

Each of the single-chip AFMs have an integrated scanner for precise movement of the probe tip in the X and Y directions and a piezoresistive sensor on the cantilever to measure the Z position of the tip and take topography measurements of the sample.[13,15–17] The sc-AFMs supports tapping mode scanning, which is useful to avoid damaging or contaminating the substrate that is being measured and unnecessarily wearing the tip as would be typical of full contact scanning. All essential components necessary to take an AFM scan are packed into a 0.25-mm^3 volume of these MEMS devices. Chevron-style thermal actuators scan the tip in X and Y, and a vertical bimorph actuates the tip in the Z axis of the sc-AFM (Fig. 3). As the physical size of the sensing and scanning components of the sc-AFMs is significantly reduced as compared to conventional tools, the sensitivity of these sc-AFM sensors and scanning systems to thermal drift and vibration is also significantly reduced. This is important because thermal drift and vibrations are major barriers to high-quality nanometrology.[2] Therefore, these sc-AFMs can
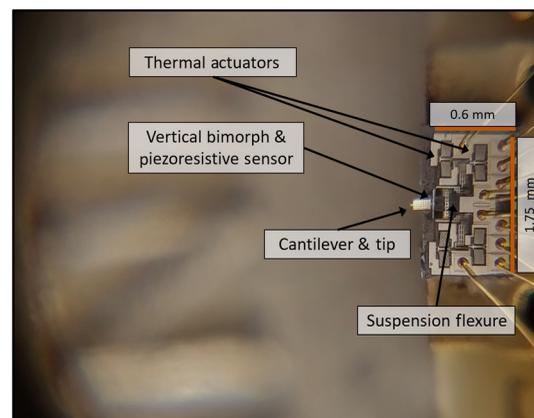

Fig. 3 sc-AFM MEMS device next to the N in united on a US quarter.

take very sensitive topography measurements of the wafer surface while operating in close proximity (<1 cm) to one another and in a nonvibration-isolated environment.

2.2 Multisite Inspection Stage Design

To enhance the metrology throughput for wafer scale measurement, the proposed system uses multiple probes distributed over the wafer footprint to image several sites simultaneously. The geometric layout of the AFMs in the system relative to a 4-in. wafer is shown in Fig. 4. Owing to the extremely small footprint of a sc-AFM system (about $1.75 \times 0.6 \times 0.4$ mm), the inspection system can equip a plurality of AFM chips within the 4-in.-diameter wafer area.[18] In this proof-of-concept hotspot inspection system, the sites are setup such that 4 sc-AFMs are placed around the periphery of the wafer with a fifth in the center. For expansion to standard 300-mm wafers, the sc-AFMs are compact enough such that each probe could measure an individual die on the wafer.

In this multisite inspection system, the sc-AFM sample approach control uses each sc-AFM cantilever sensor as a sample proximity sensor for control feedback. The piezo-resistive strain sensor detects when the sc-AFM tip begins to oscillate once it is approached within the scanning range of the probe. Proportional control (P-control) is performed duri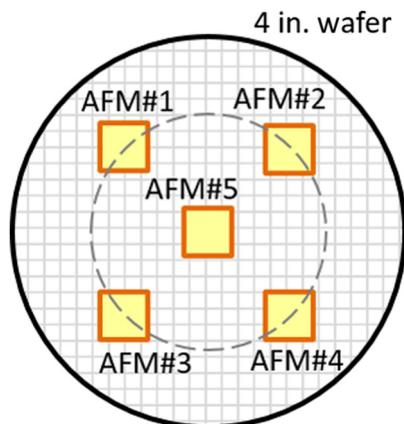ng the fine approach to ensure the AFM probe tip is correctly set at the desired measurement location and does not destructively make contact with the sample. The prototype shown in Fig. 5 employs five sc-AFMs to demonstrate the feasibility of simultaneous AFM scans using this type of experimental apparatus. The fine Z motions of the tips are controlled in parallel as every AFM measurement site has a slight difference in height, even when grounded together, due to the assembly tolerances and the topography of the wafer being measured. The system individually drives each AFM using five discrete controller-driver boards (Atmel AT91SAM). The input/output signals are carried out from these driving boards, or to the sc-AFM, by flat ribbon cables. Given the small footprint for each sc-AFM and this control architecture, it is feasible to array many more probes than the five demonstrated in this work as the computational scaling cost lies only in displaying and saving each individual scan on the master computer, all critical control is accomplished by the discrete sc-AFM driver boards. A schematic control architecture is shown in Fig. 6, where all communications between each driver and the computer are programmed and compiled using the LabVIEW software from National Instruments.

2.3 XY Motion Stage

The goal of the XY motion stage system is to precisely control the position of each sc-AFM over the desired inspection hotspot with enough range to reach a variety of hot spots within a die without adding unnecessary cost to the overall prototype system. As such, classical positioning methods such as short-range piezoelectric nanopositioning stages or high-cost linear-motor driven air-bearing stages are not considered as they would increase overall system cost by multiple orders of magnitude. The probe is thus attached to a two axis, flexure-based linear bearing coupled with VCMs. These nanopositioning stages provide about 1.3 mm of maximum unidirectional displacement in both X- and Y-directions for an overall range of ~2.5 mm in each axis. Flexure mechanisms are used in this system because, unlike conventional linear motion bearing systems that utilize rolling or sliding contacts, the flexure mechanism utilizes elastic deformation to constrain mechanism motion, which allows the mechanisms to operate without the friction and backlash issues that typically limit the repeatability of traditional motion systems.
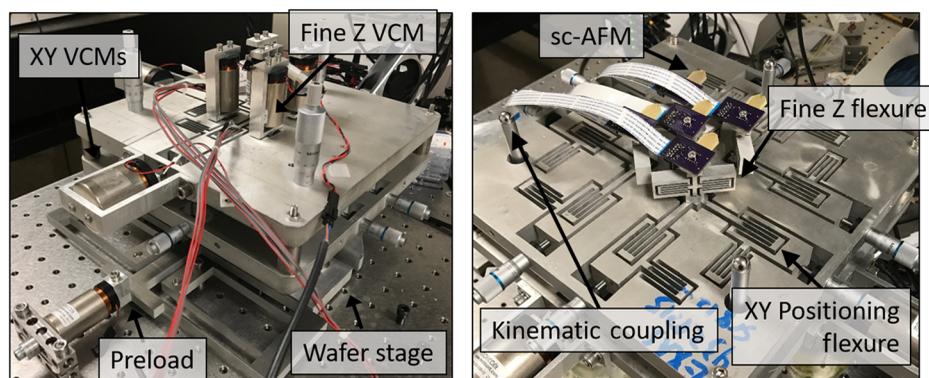
Fig. 4 Multisite metrology layout over a 4-in. wafer area.

Fig. 5 Prototype tool with major components labeled (a) an isometric view of the multisite stage assembly, including positioning VCMs and the flexure bearings and approach VCMs (b) up-side-down view of the stage assembly, showing the sc-AFMs and fine-Z probe approach flexure mechanism.
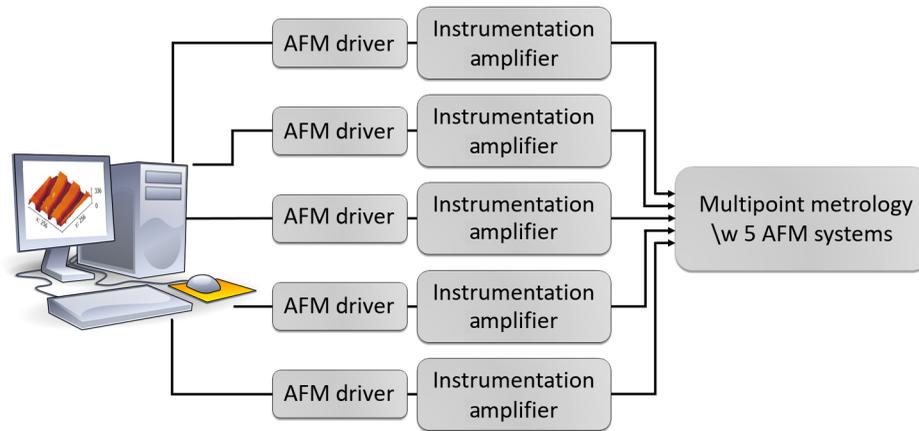
Fig. 6 Multi-AFM system control schematic.

2.3.1 *XY stage design*

The multisite inspection stages described herein leverage the general *XY* bearing design from the previously developed single-site inspection system.[12] This flexure design consists of four sets of double parallelogram flexure mechanisms, two for each axis of motion as shown in Fig. 5. By coupling these sets of flexures between a common ground, it is possible to have a center stage, which positions the sc-AFM in the desired degrees-of-freedom while constraining its motions in all other directions. The whole inspection system is located on an optical table equipped with a pneumatic isolation system, which is used to minimize the vertical and horizontal building vibrations transferred to the system in the 3- to 50-Hz frequency range (Newport ST2).

The flexure mechanisms for all the motion stages are cut from billet 7075-T651 aluminum, allowing for a very compact bearing design while avoiding assembly error. While this material is far from optimal from a thermal drift perspective, the minimal temperature fluctuation during the ∼30-s sc-AFM scan and low cost of both material and abrasive water jet cut fabrication, along with desirable Young's modulus to yield strength ratio for maximal flexure range,

outweighs this concern. The stiffness of one flexure module[19] can be written as

$$K_t \cong \left[12 - \frac{3}{100} \left(\frac{F_a L^2}{EI} \right)^2 \right] \cdot \frac{EI}{L^3}, \tag{1}$$

where L is the flexure beam length, E is the Young's modulus, I is the second moment of area for the flexure beam, and F_a is the external axial force. Equation (1) is used to parametrically design the flexure geometry in order to meet stiffness requirements. The effective stiffness of the positioning system in each direction is twice K_t due to the parallel configuration for the sets of flexures in the system. 5/8″ thick plates of were chosen for the flexure stages and were machined using abrasive water jet cutting. The arrangement of each of the five *XY* stages is based on the desired locations for the AFMs detailed in Fig. 4. For this proof-of-concept system, a two-layer design is used for the AFM stage, as seen in Fig. 7, where the flexure module for center-site motion stage is in the first layer and the surrounding four peripheral-sites motion stage located in the second layer. Those two layers are bolted together, and kinematic couplings used to
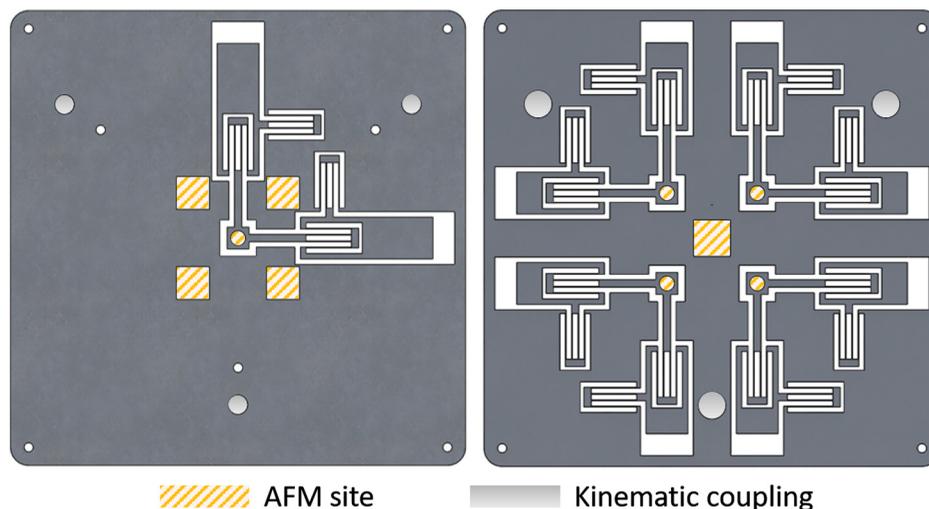

///// AFM site   Kinematic coupling

Fig. 7 Schematic of two-layered AFM stage, the flexure module for center-site motion stage is put in the first layer, the surrounded four peripheral-sites motion stage are put in the second layer.

locate the AFM stage relative to the wafer stage. The kinematic couplings are attached to the second (lower) layer to minimize the length of the mechanical path to ground and thus maximize the stiffness of the assembly.

2.3.2 XY stage motion control

Ideally, the 2-D linear stage should perform with an orthogonal coordination in motion where the X axis and Y axis are exactly perpendicular to each other. However, due to the asymmetric arrangement of flexures and imperfections in the water jet fabrication, there is typically some level of cross coupling between the two axis motions. Therefore, a parallelism test was setup to measure the parasitic error motions between the two axes. A fiber-based, interferometric measurement system (FPS3010, Attocube) with 1-pm displacement resolution was used to measure both the primary and parasitic motions of the stage while a single axis was being actuated. In this test, the wafer stage and the two interferometry probes were mechanically grounded to the optical table and a reflective rectangular block was mounted to motion stage. The results of this test are reported as a ratio of driven axis motion to undesired, free-axis cross-coupled motion. The primary drive axis motion of the stage is found to behave as a linear spring up to the signal-to-noise limit of the interferometric probe used to measure position. The cross coupling between the two axis is about 100 nm/μm, i.e., for each μm of actuated motion in one axis, there is 100 nm of undesired movement in the coupled perpendicular axis.

Although the flexure design allows the X and Y motions of the stage to be largely decoupled, this small parasitic error
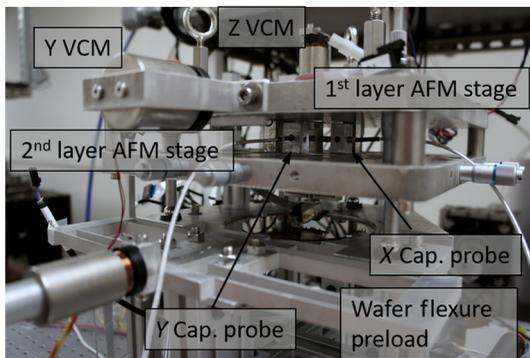

Fig. 8 Capacitance probe assembled in AFM stage for positioning sensor.

motion must still be corrected for to accurately locate the AFM probe tip over the desired inspection spot. The XY stage, therefore, uses a closed-loop proportional–integral–derivative (PID) controller to track reference inspection location and achieve nanometer-scale precision motions of the sc-AFMs within the system. The motion control system uses capacitance probes from Lion Precision (CPL 290) with 0.8-nm resolution and 250-μm working range as the sensor component in the feedback loop. Figure 8 shows the two capacitance probes mounted to the AFM stage using the square aluminum channel blocks. Each of these capacitive probes is used to measure the X or Y motion of the central stage where the sc-AFM and approach mechanism is mounted. The bearing noise due to the mechanical vibration of the system is measured by turning off the voice coil actuators and recording the signal from the capacitance probes. The overall open-loop noise in the system was measured to have a 1-sigma deviation of 4.5 nm in the X axis and 1.9 nm in the Y axis.

2.3.3 XY motion evaluation

To determine the accuracy of the positioner in closed-loop, an error motion test was performed using a 100-μm diameter error circle tracked at 0.1 Hz with a 40-Hz PID loop speed. Visual results and an error histogram, found to be taking the difference between measured position and circle reference setpoint, are shown in Figs. 9(a) and 9(b), respectively. Overall, the closed loop PID controller gives a very accurate positioning result with an average positioning error of 6.2 nm and a root mean squared positioning error of 4 nm. The motion test demonstrates that the XY probe positioning error is small enough compared to the FOV of the sc-AFM system such that the probe tip can easily be aligned with the desired measurement area on the wafer in a rapid manner—a key requirement for in-line inspection. In addition, the performance of this positioning system enables the sc-AFM probe to be accurately moved after one measurement is completed to an adjacent location where another scan can be taken with a precisely controlled amount of overlap with the first image. Repeating this procedure several times results in consecutive images that, after the application of an offline stitching algorithm, can be combined into a single large topography scan—significantly enhancing the FOV of the metrology system.

2.4 Wafer Loading and Inspection Cycle

The wafer to be evaluated is transported into the system for cycle speed testing by a custom wafer handling robot driven
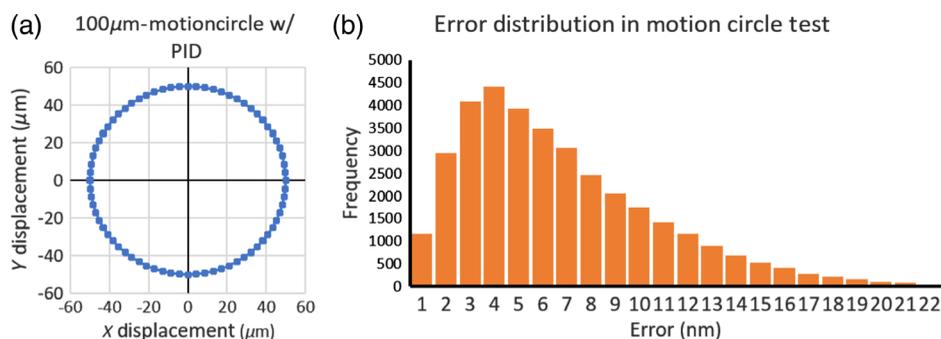

Fig. 9 (a) 2-D circle motion driving test in a 100-μm circle around the origin, the average positioning error is about 6.2 nm and (b) error distribution in positioning in 100-μm circle tracking test.

by open-loop stepper motors in an automated fashion.[20] The subsystem consists of motor driven elevator and rotary stages and a vacuum chuck handle, which removes 4-in. wafers from a storage cassette before transport and loading into the wafer capture stage. Once captured, a passive alignment mechanism using three pins around the wafer constrains the wafer position with respect to the sc-AFM proves to submicron-level precision for scanning. The wafer loading system currently runs in open-loop, which dictates the use of relatively slow travel rates to reduce positioning errors caused by system dynamics—especially when compared to industrial rapid wafer handling robots. An off-the-shelf solution of a faster, closed-loop system could be implemented to decrease inspection cycle time.[21]

2.5 AFM Image Correction

Postprocessing is used to level sc-AFM images, convert from the polar scan coordinates inherent to the sc-AFM motion mechanism to the Cartesian coordinates of the desired image, and register the scan coordinate system to the wafer coordinates of the desired hot spot. The leveling must take place to correct for the inclination of the sc-AFM mount and repeatability errors in the kinematic coupling between the wafer capture stage and sc-AFM nanopositioners. In addition, any drift of tip height relative to the sample will result in feature drift in the image. Fortunately, both the tilt and tip drift can be compensated for using a polynomial fit in both row and column directions to define the background inclination and subtract it from the scan.[22]

As the sc-AFM uses a flexure-based nanoscanner anchored to a single point to actuate the tip for scanning, the nature of this mechanism results in an arc-like motion. Thus in addition to the leveling, the other major postprocessing step is to convert images from the square, rasterized pixel map reported by the controller-driver to the polar scan axes of the sc-AFM. When the arm length from the probe tip to its pivot is much longer than the scanning range, the annular sector formed by this scanning can be seen as rectangular and is reported as a square, rasterized scan by the sc-AFM controller-driver. To correct the square pixel map of the polar scanning motion and create a final image, a geometric analysis must be employed, as shown by the exaggerated schematic in Fig. 10.

Beyond correcting for the tilt and polar nature of the collected data, the scan axis of the sc-AFM itself must also be registered to the desired coordinate access of the wafer. Due
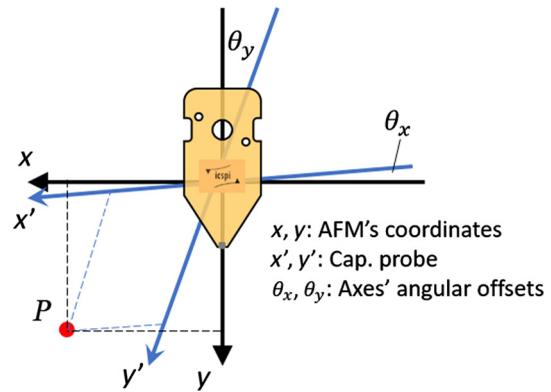

Fig. 11 Schematic of axes mismatch from the assembly tolerance of capacitance probe installation.

to the assembly tolerances of the sc-AFMs, the capacitance probes mounted on the AFM stage may not be perfectly aligned with the sc-AFM's reference axis or the axis of the wafer patterns, which will cause the image to appear to drift as the sc-AFMs are moved between different imaging sites. This is shown in Fig. 11, where the assumed scanning motion of sc-AFM conforms to an orthogonal coordinate system, but the installation of X and Y-capacitance probes introduce some rotational errors resulting in an angular offset. Therefore, even though the PID controller provides a precise and accurate positioning of the sc-AFM probes, the motion is based on the capacitance probes' reference angles, which may have some angle with respect to the actual desired scan axis. It is, therefore, necessary to transform this capacitance-based motion to coincide with the AFM.

The angles θ_x and θ_y represent the angular offsets between the horizontal axis and X-capacitance (denoted as x' in schematic) and the vertical axis and Y-capacitance (denoted as y' in schematic), respectively. The transformation matrix from the capacitance coordinate system to AFM's reference can be written as shown in Eq. (2).

$$\begin{pmatrix} x \\ y \end{pmatrix} = \begin{pmatrix} \cos\theta_x - \sin\theta_x \tan\theta_y & \sin\theta_y \\ \sin\theta_x & \cos\theta_y - \sin\theta_y \tan\theta_x \end{pmatrix} \times \begin{pmatrix} x' \\ y' \end{pmatrix},$$

(2)

where x and y are the coordinates represented to the reference of sc-AFM, x' and y' are those represented to the capacitance
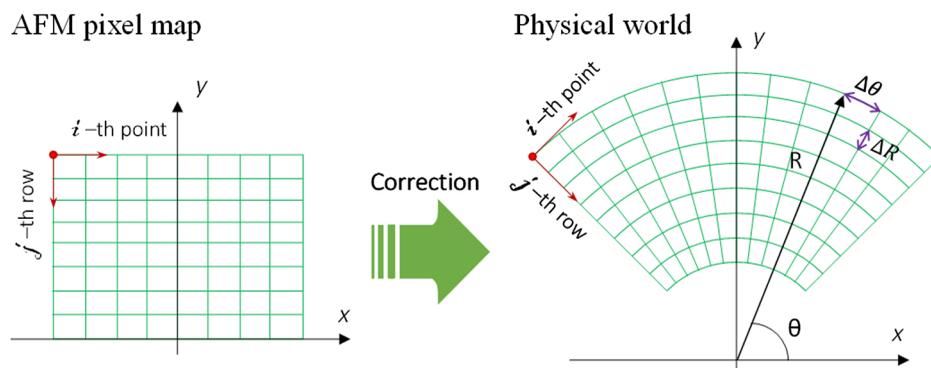

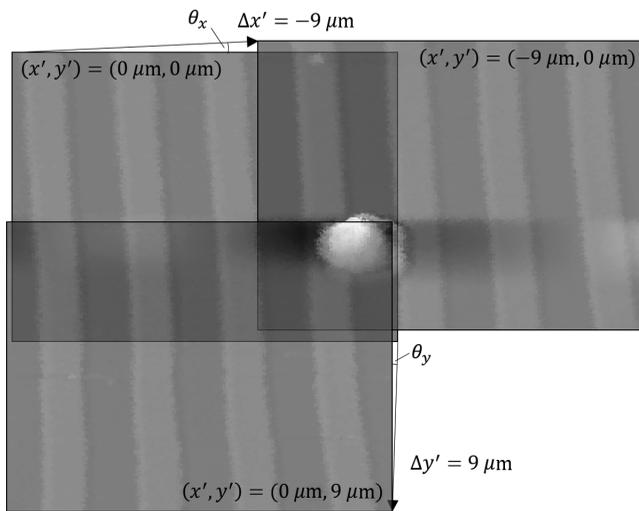**Fig. 10** A schematic of the sc-AFM scan axis correction principle.

Fig. 12 A test shows the axes mismatch between capacitance axes and sc-AFM.

Fig. 13 Position offset of the lithography area registered on wafer. The black dashed line shows where the photolithography area should be, it is supposed to be centered at wafer center. The red dashed line shows the actual location of the photolithography area.

Fig. 14 Strategy to register the lithography area before inspection starts.

axes. The angles θ_x and θ_y are extracted by tracking the location of a feature of interest, such as a speck of dust or an impurity spot on the sample, between different coordinated scans as shown in Fig. 12.

To calibrate the angular offset between the AFM's scan axis and the sample axis, the point of interest is first located relative to the origin of the first scan and after taking the first scan at the origin, the motion stage moves in the x'- and y'-directions with a known displacement before taking scans at each of these new points. These images are overlaid with the feature of interest acting as an anchor point. As a result, the angular offsets can be calculated using Eqs. (3) and (4) from the displacements of the AFMs measured by the capacitance probes ($\Delta x'$ and $\Delta y'$) and the parasitic error motions on the images ($\delta y_{x'}$ and $\delta x_{y'}$)

$$\theta_x = \sin^{-1} \frac{\delta y_x}{\Delta x'}, \tag{3}$$

$$\theta_y = \sin^{-1} \frac{\delta x_y}{\Delta y'}. \tag{4}$$

3 Locating Hotspots on Wafer

Semiconductor nanofabrication processes typically rely on fiducial marks for the tracking of each layer's pattern position relative to the wafer geometry coordinate frame between different fabrication steps. As such, points of interest for inspection based on *a priori* knowledge can be located within the pattern on the wafer relative to the tracked location of the fiducial marks once the wafer has been captured and passively aligned by the proof-of-concept system.[14] A schematic representation of this difference in alignment of pattern to wafer is shown in Fig. 13.

As the precise orientation of the pattern with respect to the wafer flat will vary with each individual wafer, a method for correction must be made to locate exact features on a patterned wafer. A typical strategy, outlined in Fig. 14, is to use the fiducial mark in the pattern to register the lithography area to the wafer edges. A high-resolution camera is often used to measure the fiducial marks' locations relative to the centroid of the wafer in the captured image. An offset can
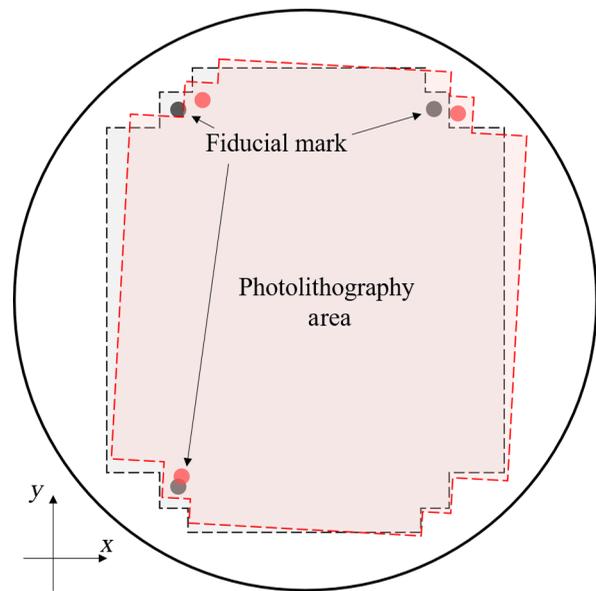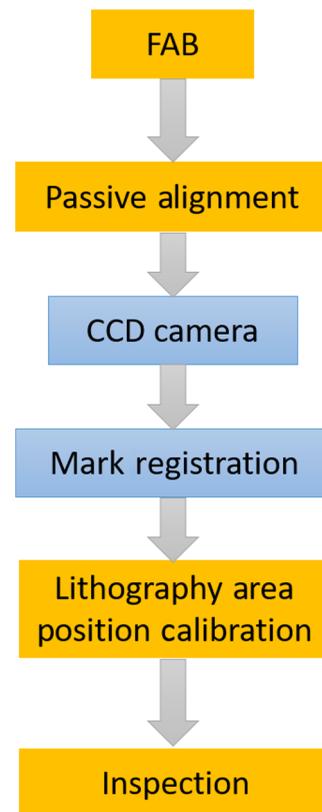
then be calculated between the actual location of the fiducial marks and the theoretical location of the marks if the pattern was perfectly centered on the wafer. This offset can then be added to the known locations of the inspection hotspots so that the AFM probe tips can be positioned directly above the
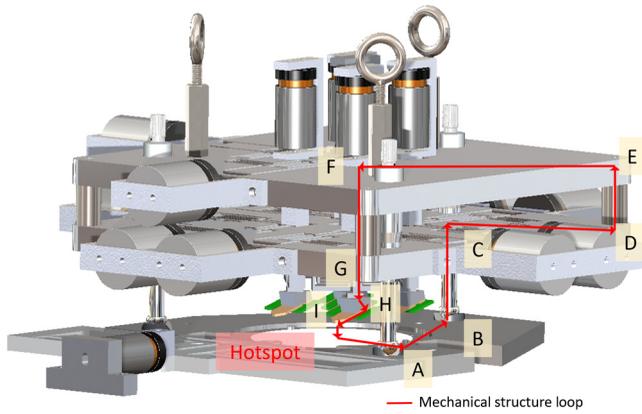
Fig. 15 Mechanical structure loop from the measurement spot on the wafer to the AFM tip above, passing through A, wafer alignment pin; B, kinematic coupling block; C, micrometer bolt on second layer inspection stage; D, spacer bottom; E, spacer top; F, 2-D motion stage; G, z-flexure; H, sc-AFM holder; and I, AFM tip.

Fig. 16 Schematic of AFM alignment angular error caused by the clearance between pin and hole.

desired inspection area in the metrology system. For the 4-in. wafers used in this proof-of-concept tool, the uncertainty in the offset measurement is about 2 μm, which is significantly less than the FoV of the sc-AFMs ensuring that the desired hotspots will be within the imaging area of the metrology system after each cycle.

In addition to the offset error, the accuracy with which the wafer is loaded into the 3-pin alignment system or the repeatability of the kinematic coupling system used to mate the wafer stage to the AFM stage adds uncertainty to the calculated position of patterned structures. A full mechanical loop of the tool starting from a predefined hotspot to the sc-AFM probe tip is shown in Fig. 15. In an ideal assembly, the probe tip would be perfectly co-located with the desired hotspot for inspection. Homogeneous transformation matrices (HTM)[13,23] are used to translate the coordinate system of the AFM tip from the reference (hotspot location) on the wafer to its actual assembled position in the inspection stage. Starting with the wafer stage coordinate system, translational transformations take the form shown in Eq. (5) with rotational errors represented by the epsilon terms and the subscript of each term, indicating the axis about which the rotation occurs[14]

$$
{}^{R}T_N = \begin{bmatrix} 1 & -\varepsilon_z & \varepsilon_y & a+\delta_x \\ \varepsilon_z & 1 & -\varepsilon_x & b+\delta_y \\ -\varepsilon_y & \varepsilon_x & 1 & c+\delta_z \\ 0 & 0 & 0 & 1 \end{bmatrix},
\tag{5}
$$

where a, b, and c represent large translations, δ_x, δ_y, and δ_z are the translational error motion, and the subscripts indicate the directions. The whole system can, therefore, be decomposed into a series of coordinate transformation matrices that describe the relative position of each pair of connected parts relative to adjacent nodes in the structural loop to assist the modeling process. Assuming N parts are connected in series and the relative HTMs of each connected part are known, the position of the AFM tip relative to the hotspot location (0'th part in this series and N'th part is the AFM tip) will be the sequential product of all the HTMs, shown as in
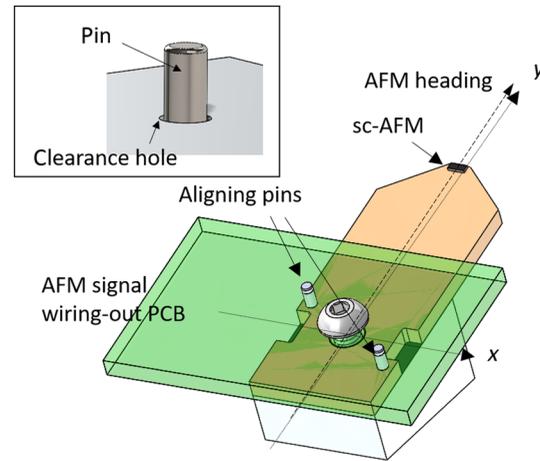
$$
{}^{0}T_N = \prod_{i=1}^{N} {}^{i-1}T_i.
\tag{6}
$$

Translational and rotational errors in each HTM depend on the assembly tolerances, machining tolerances, or the coupling repeatability of the part being described by the HTM. The uncertainty in height (Z direction) is mainly due to the four standard spacers between top and bottom AFM stages. However, this is a nonsensitive direction since errors in the AFM height can be compensated during the AFM approach procedure. In contrast, the errors in the X and Y directions directly result in an offset between the desired imaging area and the actual area that is scanned and, therefore, must be examined more precisely. The largest error in the X and Y directions is the result of the uncertainty in the angular alignment of the sc-AFM mounting. Each sc-AFM is loaded into the metrology system using a 2-pin alignment system and is then bolted in place, a cartoon representation of this is detailed in Fig. 16. Since the pin holes in the sc-AFM board are larger than the pins themselves to make the probe easy to load onto the metrology system, there exists uncertainty in the exact location and angle of the sc-AFM board relative to the rest of the metrology system. However, once the sc-AFM is bolted in place, it does not move again until the chip needs to be replaced.

The error in location and angle of the cantilever tip relative to the wafer geometry system can be measured with a known test artifact wafer, and a calibration offset added to the XY position command of each the sc-AFM positioner stages. Given this calibration and the precision of the nanopositioning stages, the overall repeatability can be made to match that of the system without any appreciable AFM alignment error. Thus the major limits on the repeatability of the system are the image offset uncertainty, wafer loading repeatability in the 3-pin passive alignment system, and repeatability of the kinematic coupling locating the AFM stage to the wafer stage. The overall error in the location of the probe tip relative to the hotspot being measured is found to be ∼3.5 μm (combined X and Y error) (Table 1). This error is significantly less than the FoV of the sc-AFM, roughly 20 μm × 20 μm, which ensures that the desired hotspot can be imaged using this metrology system without the

Table 1 Random positional error of AFM tip in system assembly.

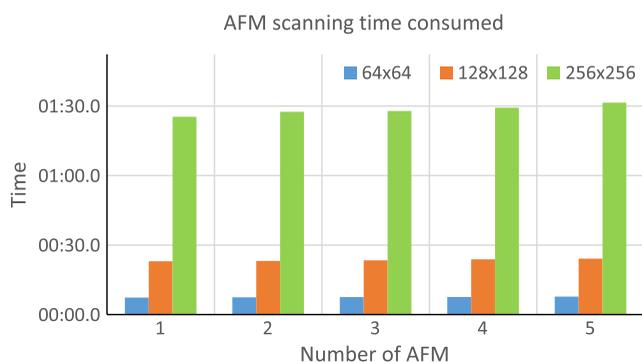| Direction	X	Y	Z
Error (μm)	44.50	167.1	254.7
Error without AFM alignment error (μm)	2.880	2.052	210.5

need for any postloading alignment steps, which is a critical requirement to achieve the necessary throughputs of an inline metrology system for the semiconductor industry.

4 Large Area Measurements

4.1 Multisite Hotspot Inspection

In preliminary testing for multisite measurement, Fig. 17 shows the sc-AFM scan operation time with different numbers of parallel scanning probes employed by the proposed system and at various pixel densities. As can be seen, the number of sc-AFMs scanned does not have any significant effect on the overall measurement time. The slight increase in scan acquisition time is most likely attributed to the additional overhead in simultaneously processing and displaying each scan in LabVIEW in real time, not from any physical limitations of the sc-AFM controller/driver. In terms of throughput, the proposed system operates on the time budget outlined in Table 2, where total inspection cycle time is <1 min, leading to a metrology throughput of ~66,000 μm^2/h.

To demonstrate that there are no significant noise sources inherent to simultaneous sc-AFM scanning that could affect each individual measurement, five grating samples of 3-μm pitch and 92.5 ± 2.5 nm height (Ted Pella, TGZ2) were placed below the probes and measured in parallel. The multi-AFM scanning results with a 512 × 512 pixel scans are shown in Fig. 18. As preproduction sc-AFM sample probes were used in this work, the FOV on each scan is about

17 μm × 12 μm as opposed to the final sc-AFM FOV of 20-μm square and sensitivity of the vertical piezoresistive sensor more variable compared to production quality devices. There is almost no measurable delay in execution time between the system operating with one probe or simultaneously scanning with five sc-AFMs. Overall, these scans show that the multiple sc-AFMs can be run in parallel without reduction in scan quality or increase in scan time.

Thus given the data flow configuration of this system, the maximum number of AFMs that can operate in parallel is limited only by the physical dimensions of each sc-AFM device and wire-bond board, unlike more typical, larger, laser-sensed AFM tools. The MEMS sc-AFM itself is only about 1.75 × 0.6 mm, extremely small in the context of the even compact (usually 10s of mm) macroscale scanning stages utilized in classical AFM tools—allowing for an even higher probe density ceiling. The proof-of-concept prototype presented in this paper to demonstrate the feasibility of multisite measurement utilizes sc-AFM chips bonded onto a wire bond PCB, which is about 30 × 12 mm in size. As such, in order to further maximize the number of AFMs that could be arrayed in a metrology system, the PCB daughter boards could be redesigned to allow for flip chip assembly of the sc-AFMs to the PCBs, which would help reduce footprint to ~10 × 10 mm. Such a PCB design would enable up to 78-site measurements to be taken on 4-in. wafer simultaneously and up to 700 site parallel measurement to be made on a 300-mm wafer without increasing the overall inspection cycle time. This would result in a theoretical maximum inspection throughput of ~1 mm^2/h on a 4-in. wafer and ~9.25 mm^2/h on a 300-mm wafer. In practice, these throughputs would be more than sufficient for the multihotspot inspection typically required for inline wafer metrology in fabrication facilities.

4.2 Large Single-Site Measurement

Once a defect has been identified during the hotspot inspection, it can be advantageous to inspect the areas around the original region of interest to construct a more complete picture of the potential fabrication errors in the wafer. Large area measurements can be performed using the sc-AFM by repositioning the probe with the XY nanopositioner and algorithmically stitching together the adjacent scans. Image stitching has been widely used in many applications such as panorama photography, 360-deg video production, and motion estimation techniques. In the image stitching process shown in Fig. 19, images are acquired in a square grid where each scan overlaps its adjacent neighbors. After all regions are scanned, the in-line metrology system automatically processes the image corrections (sample-probe alignment tilting, scanning coordinates artifact, and sensor aligning angular offsets) and stitches the images together using a correlation algorithm to form an expanded FOV topography reconstruction of the sample.

Fig. 17 Scan times for various numbers of parallel scanning sc-AFM devices.

Table 2 Measured budget for each step in a typical hot-spot inspection cycle. A cycle consumes <1 min.[12]

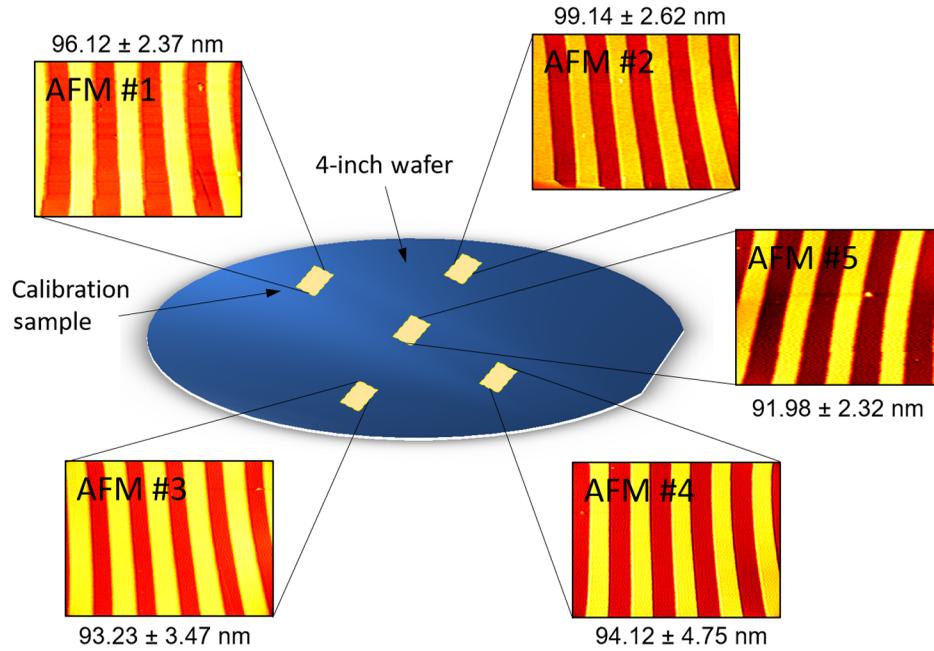|	Startup cycle wafer loading	Stage lift and lower	AFM approach	Scan	AFM retract	Stage lift and lower	Wafer exchange
Time budget (s)	7.07	0.095	5.31	26.05	0.07	0.095	20.55

Fig. 18 Multisite hotspot measurement result for 5 sc-AFMs scanning in parallel (512×512 pixel resolution).
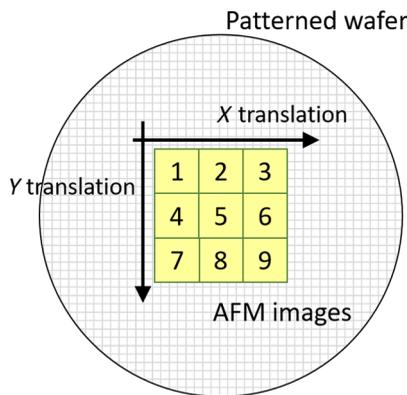

Fig. 19 A schematic of image-stitching mosaic.

4.2.1 Image registration

Phase correlation is used to track a specific feature's displacement from one image to the next for stitching alignment. It relies on Fourier analysis and is fast to execute but is also sensitive to noise in the signal.[24–30] Fortunately, sc-AFM images typically exhibit very good signal-to-noise ratios, so a phase correlation algorithm was effective in registering adjacent sc-AFM images. In the phase correlation algorithm, where $f_1(x, y)$ and $f_2(x, y)$ are the two datasets to be stitched together, and assuming there is only translational relation between the two images,[28] i.e., $f_2(x, y) = f_1(x - \Delta x, y - \Delta y)$, the Fourier shift between the two data sets is given by

$$F_2(\omega_x, \omega_y) = F_1(\omega_x, \omega_y)e^{-i(\omega_x \Delta x + \omega_y \Delta y)}. \tag{7}$$

The Fourier transforms of the two images have a phase difference, which is directly related to the relative displacement between the two images. Therefore, the normalized cross power spectrum retaining the phase difference information is defined as

$$\frac{F_1(\omega_x, \omega_y)F_2^*(\omega_x, \omega_y)}{|F_1(\omega_x, \omega_y)F_2^*(\omega_x, \omega_y)|} = e^{-i(\omega_x \Delta x + \omega_y \Delta y)}, \tag{8}$$

where $F^*(\omega_x, \omega_y)$ is the complex conjugate of $F(\omega_x, \omega_y)$. By taking the inverse Fourier transformation of Eq. (8), a Dirac delta function centered at the location that represents the displacement between the two images can be derived given Eq. (9). This process can be repeated for subsequent scans to determine overall image grid translations and final scan locations for optimal image stitching

$$P(x, y) = \mathcal{F}^{-1}\left[\frac{F_1(\omega_x, \omega_y)F_2^*(\omega_x, \omega_y)}{|F_1(\omega_x, \omega_y)F_2^*(\omega_x, \omega_y)|}\right]$$
$$= \delta(x + \Delta x, y + \Delta y). \tag{9}$$

4.2.2 Image blending

One of the largest challenges in stitching together adjacent images lies in the edges or seams that can be created within overlapped regions of stitched images, usually due to the intensity discrepancies present even when the feature registration process described in the previous section is executed perfectly.[25] Therefore, an image blending, or "feathering," algorithm is needed to remove those seams and smooth the stitching area. Feathering quantitatively investigates the intensity characteristics on both images to increase coherence with each other. The feathering algorithm used in this work operates by first locating the position of the maximum intensity gap between the two stitched images exists (i.e., the seam line). Then assuming W is the feathering radius and $w(x, y)$ is the feathering weight function, the final image $I(x, y)$ is blended from images $I_1(x, y)$ and $I_2(x, y)$ as defined in

$$I(x, y) = w(x, y)I_1(x, y) + [1 - w(x, y)]I_2(x, y), \qquad (10)$$

where $w(x, y)$ is defined by $d(x, y)$, which is the straight-line distance between the pixel (x, y) and the seamline

$$w(x, y) = \frac{W \pm d(x, y)}{2W}. \qquad (11)$$

The sign in Eq. (11) depends on which side of the seam line the pixel located on. It is positive if it is on the I_1 side of the image and negative if it is on the I_2 side of the image. At the seamline, the pixel value is simply an average of the two images.

4.2.3 Large area measurement results

To validate the large-area capability of the proposed inspection system, a 3×3 measurement grid was taken of a standard calibration grating (Ted Pella, TGZ2) with each image separated from its neighbor by 10 μm such that there is about 5 μm of overlap between images. The stitching algorithm including feature registration and image-blending was then applied to the images, and the final resultant image is shown in Fig. 20. The final dimensions of the 3×3 stitched image are about 32.4 μm on X axis and 37.7 μm on Y axis, which is about a 5.5-times the expansion of the original FOV of the sc-AFM. Overall, this demonstration shows image stitching can be used to further investigate larger areas around defects found during the initial hotspot inspection of the wafer for root-cause analysis and other further investigation.

An exemplary expanded-area scan stitched from the central sc-AFM in the prototype system is shown in Fig. 21
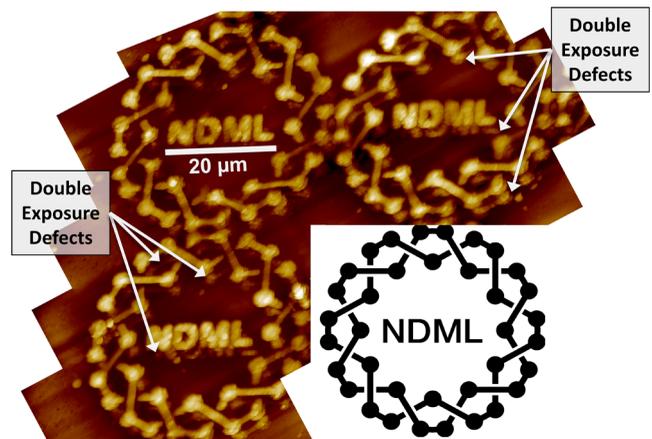

Fig. 21 Stitched mosaic of 400 nm tall reproductions of the NDML logo additively manufactured with a two photon polymerization process showing difficult-to-quantify double exposure printing defects.

(topoStitch, Image Metrology A/S). Here, a two-photon polymerization additive manufacturing process (NanoScribe) is used to print an array of Nanoscale Design and Manufacturing Laboratory (NDML) logos on a glass substrate. As experimental process parameters were utilized, some prints experience "double-exposure" defects where the logo is printed twice, one over the other, with a primary pattern prominently seen and a short, "ghost" or "shadow" pattern visible directly adjacent to most of the features in two of the three arrayed pattern prints. These types of printing defects, while generally difficult to monitor and quantify
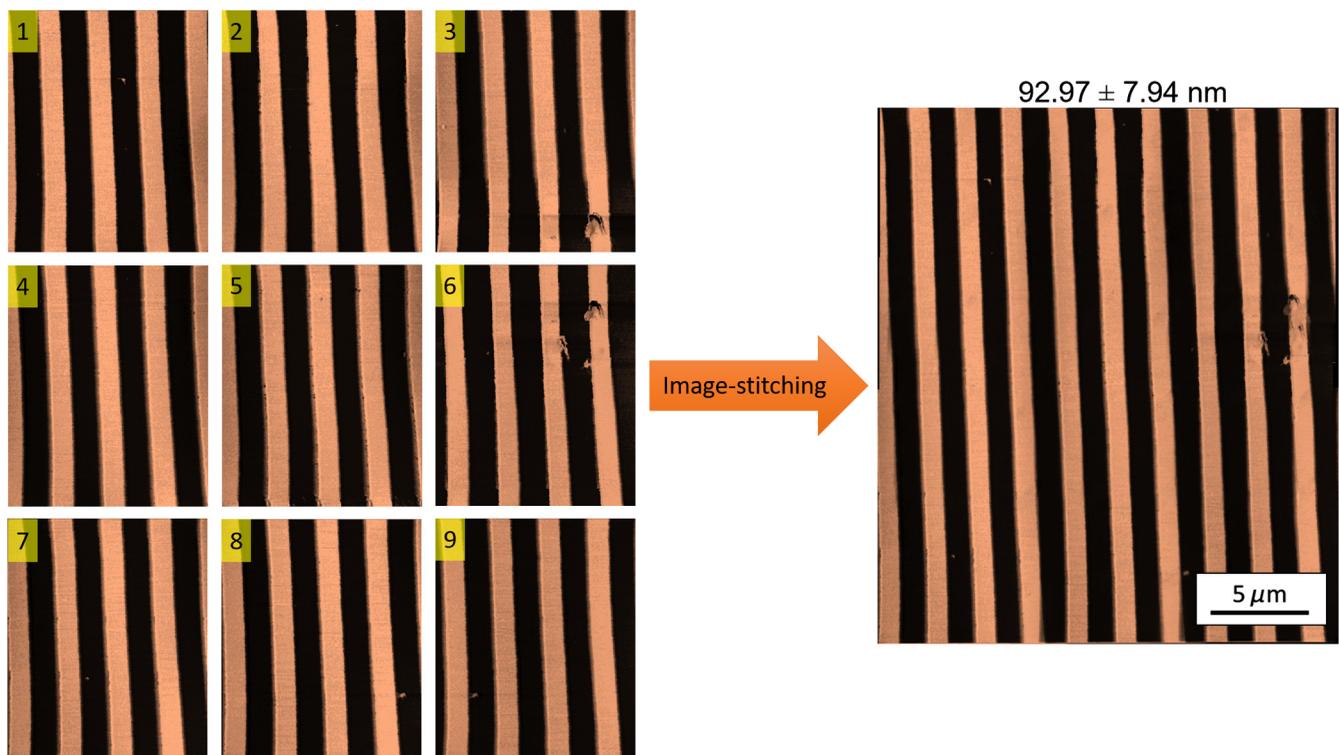

Fig. 20 Resultant image after correction, registration, and image-blending algorithms to stitch all the 9 images into one single image. The final dimensions are about 32.4 μm in the X axis and 37.7 μm in the Y axis.

with optical methods, are easily seen in this roughly 0.1 mm × 0.1 mm L-shaped stitch.

5 Conclusion

The proof-of-concept multipoint hotspot inspection system presented herein implements a plurality of sc-AFM probes over a single wafer, where each sc-AFM is responsible for imaging a single hotspot, and the distribution and location of each scan site is set according to offline hotspot map. Each probe can be positioned in the $X–Y$ plane above the wafer with nanometer-scale precision to measure specific features beyond the diffraction limit of visible light. With the current sc-AFM array, a speed of 60 WPH for hotspot inspection of five points on a 4-in. wafer specimen is achieved, which corresponds to a measurement throughput of 66,000 μm^2/h. Further, the compact physical packaging of the sc-AFM and demonstrated parallel measurement capability makes it feasible to incorporate up to 78 probes over a 4-in. wafer, leading to a theoretical limit of up to 1.03 mm^2/h within one 60-s inspection cycle. If a standard 300-mm wafer specimen was to be measured, the number of sc-AFMs in the array can be further increased to a maximum of 700 hotspots for a theoretical metrology throughput of 9.27 mm^2/h.

This methodology for in-line inspection could, therefore, be used to detect "killer" defects and measure subwavelength CDs with significantly improved throughput compared to current off-line scanning probe microscope systems, most of which employ a single tip. In a hybrid metrology framework where traditional CD-SEM and CD-AFM tools are utilized for the most demanding, sub-7-nm node CD measurements, and optical inspection for locating larger defects, the proposed system can fill this gap between the two extremes of current semiconductor fab metrology capabilities. This would allow for process feedback decisions to be made with significantly more data available, which can enhance existing statistical process control model accuracy and response to process variation to improve the overall fabrication yield. Moreover, once a defect is detected, the system can also perform a more detailed, off-line review of a large region surrounding the defect by algorithmically stitching together multiple scans in a grid. The resulting expanded FOV scan preserves fidelity of any nanoscale topography measured and can be used to determine the underlying cause of any detected killer-defects in the pattern with the aim of preventing future similar defects from occurring and lowering overall yield.

References

1. G. E. Moore, "Cramming more components onto integrated circuits, Reprinted from Electronics, volume 38, number 8, April 19, 1965, pp. 114 ff," *IEEE Solid-State Circuits Soc. Newsl.* **11**(3), 33–35 (2006).
2. N. G. Orji et al., "Metrology for the next generation of semiconductor devices," *Nat. Electron.* **1**, 532–547 (2018).
3. A. Vaid et al., "In-line E-beam wafer metrology and defect inspection: the end of an era for image-based critical dimensional metrology? New life for defect inspection," *Proc. SPIE* **8681**, 86810D (2013).
4. W. L. Vos et al., "Scattering lens resolves sub-100 nm structures with visible light," *Phys. Rev. Lett.* **106**, 193905 (2011).
5. S. Weisenburger and V. Sandoghdar, "Light microscopy: an ongoing contemporary revolution," *Contemp. Phys.* **56**, 123–143 (2015).
6. R. Heintzmann and G. Ficz, "Breaking the resolution limit in light microscopy," *Methods Cell Biol.* **114**, 525–544 (2013).
7. R. Neubecker and J. E. Hon, "Automatic inspection for surface imperfections: requirements, potentials and limits," *Third Eur. Semin. Precis. Opt. Manuf.* **10009**, 1000907 (2016).
8. B. Thiel et al., "Assessing the viability of multi-electron beam wafer inspection for sub-20 nm defects," *Proc. SPIE* **9236**, 92360E (2014).
9. C. Bruker, Bruker AFMs for semiconductor metrology, 2019, https://www.bruker.com/products/semiconductor-metrology/automated-afm.html.
10. R. Buengener, "Defect inspection strategies for 14 nm semiconductor technology," *Proc. SPIE* **8466**, 846607 (2012).
11. P. Vettiger et al., "The "Millipede"—more than thousand tips for future AFM storage," *IBM J. Res. Dev.* **44**, 323–340 (2000).
12. T. F. Yao, A. Duenner, and M. Cullinan, "In-line metrology of nanoscale features in semiconductor manufacturing systems," *Precis. Eng.* **47**, 147–157 (2017).
13. N. Sarkar, G. Lee, and R. R. Mansour, "CMOS-MEMS dynamic FM atomic force microscope," in *17th Int. Conf. Solid-State Sens. Actuators and Microsyst. (Transducers & Eurosensors XXVII)*, pp. 916–919 (2013).
14. A. Duenner and M. A. Cullinan, "Passive semiconductor wafer alignment mechanism to support in-line atomic force microscope metrology," in *ASPE 2015 Annu. Meet.* (2015).
15. N. Sarkar et al., "A 0.25 mm^3 atomic force microscope on-a-chip," in *28th IEEE Int. Conf. Micro Electro Mech. Syst. (MEMS)*, IEEE, pp. 732–735 (2015).
16. D. Strathearn et al., "The benefits of miniaturization of an atomic force microscope," in *Proc. IEEE Int. Conf. Micro Electro Mech. Syst.*, pp. 1363–1366 (2017).
17. N. Sarkar et al., "A platform technology for metrology, manipulation and automation at the nanoscale," in *Int. Conf. Manip. Autom. Robot. Small Scales, (MARSS 2017)* (2017).
18. N. Sarkar et al., "CMOS-MEMS atomic force microscope," in *16th Int. Solid-State Sens. Actuators Microsyst. Conf. TRANSDUCERS'11*, pp. 2610–2613 (2011).
19. S. Awtar and G. Parmar, "Design of a large range XY nanopositioning system," *J. Mech. Robot.* **5**, 021008 (2013).
20. A. Duenner et al., "A low-cost, automated wafer loading system with submicron alignment accuracy for nanomanufacturing and nanometrology applications," *J. Micro Nano-Manuf.* **4**, 041006 (2016).
21. W. Aribowo et al., "Vibration control of semiconductor wafer transfer robot by building an integrated tool of parameter identification and input shaping," *IFAC Proc.* **44**, 14367–14373 (2011).
22. P. Eaton and P. West, *Atomic Force Microscopy*, Oxford University Press (2010).
23. A. Slocum, *Precision Machine Design*, Society of Manufacturing Engineers, Southfield, Michigan (1992).
24. J. P. Lewis, "Fast template matching," in *Vis. Interface*, pp. 120–123 (1995).
25. R. Szeliski, "Image alignment and stitching: a tutorial," *Found. Trends Comput. Graph. Vision* **2**, 1–104 (2006).
26. S. Johar, G. R. Manjula, and M. V. Namita, "Image stitching using correlation method," *Imperial J. Interdiscip. Res.* **3**, 282–290 (2017).
27. S. Zhao and Q. Yang, "A stitching method for AFM based large scale scanning with high resolution," *IFAC Proc.* **47**, 2697–2702 (2014).
28. H. Foroosh, J. B. Zerubia, and M. Berthod, "Extension of phase correlation to subpixel registration," *IEEE Trans. Image Process.* **11**, 188–200 (2002).
29. L. G. Brown, "A survey of image registration techniques," *ACM Comput. Surv.* **24**, 325–376 (2002).
30. R. Szeliski and H.-Y. Shum, "Creating full view panoramic image mosaics and environment maps," 251–258 (2005).

Tsung-Fu Yao received his BS and MS degrees in mechanical engineering from National Taiwan University in 2010 and 2011, respectively, and his PhD in mechanical engineering from The University of Texas at Austin in 2018. He is the author of more than 10 technical articles and 2 pending patents. His research interests include nanopatterning process, nanoscale motion mechanism, and high-volume inspection for nanomanufacturing.

Liam G. Connolly received his BS degree in mechanical engineering from Tufts University, Medford, Massachusetts, USA, in 2016 and his MS degree from The University of Texas at Austin in 2019. He is currently pursuing his PhD in the Walker Department of Mechanical

Engineering at The University of Texas at Austin. His current research interests include precision machine design for nanometrology, roll-to-roll nanofabrication, real-time control design, and microscale roll-to-roll web modeling.

Michael Cullinan received his BS degree in mechanical engineering, his BA degree in economics from Swarthmore College, Swarthmore, Pennsylvania, USA in 2006, and his MS and PhD degrees in mechanical engineering from Massachusetts Institute of Technology, Cambridge, MA, USA, in 2008 and 2011, respectively. He is currently an assistant professor and the director of the Nanoscale Design and Manufacturing Lab at UT Austin. Prior to joining the University of Texas, he was a national research council postdoctoral associate at the National Institute of Standards and Technology in Gaithersburg, Maryland, USA. His research interests include the design and development of nanomanufacturing processes and equipment, the application of nanoscale science in engineering, the engineering of thin films, nanotubes, and nanowires, the manufacturing and assembly of nanostructured materials, and the design of micro/nanoscale machine elements for mechanical sensors and energy systems.